A Convolution Model for Earthquake Forecasting Derived from Seismicity Recorded During the ST1 Geothermal Project on Otaniemi Campus, Finland

Jean-Philippe Avouac[1,2], Maxime Vrain[2], Taeho Kim[1], Jonathan Smith[1], Thomas Ader[3], Zachary Ross[1], Tero Saarno

[1]Geomechanics and Mitigation of Geohazards, California Institute of Technology, Pasadena, California, USA

[2]Laboratoire de Mécanique du Solide, Ecole Polytechnique, Palaiseau, France

[3]Arup, 13 Fitzroy Street, W1T 4BQ, London, UK London

avouac@gps.caltech.edu

ABSTRACT

We analyse and model the spatio-temporal evolution of seismicity induced by hydraulic stimulations at 6.1 km deep over 50 days during an EGS development on Aalto University's Otaniemi campus. We use the records from surface accelerometers and borehole seismometers installed at depth between 0.3 and 2.7km. The data were processed using Machine Learning techniques for phase detection (the Generalized Phase Detection), a back-projection technique for phase associations and location (Quake Migrate). Relative locations were refined using a cross-correlation techniques. The procedure yielded a catalog of ~70,000 events, including ~10,000 events which could be located precisely. Local magnitudes between range between -1.5 and 2. We investigate how the seismicity relates in time and space to the injection history. We find that the evolution of the seismicity in time can be successfully represented using a simple convolution model. The parameters of the model are calibrated from the seismicity data themselves, in particular the Omori-like decay of seismicity observed during shut-in periods. We use a simple physics-based simulator which assumes linear-pore pressure diffusion and earthquake nucleation governed by a standard Coulomb failure model to assess the validity of the convolution model approximation. This approach could in principle be used for time-dependent seismic hazard assessment, to feed a traffic light system or eventually for optimization and control during stimulation or operation of a geothermal well.

1. INTRODUCTION

Seismicity is commonly associated to the development and operation of geothermal fields (e.g., Majer *et al.*, 2007, Gaucher *et al.*, 2015, Elsworth *et al.*, 2016, Zang *et al.*, 2014). This is intended when hydraulic stimulation is needed to enhance the heat exchange between the circulating fluids and the reservoir rocks with the creation or reactivation of fractures. Seismicity is therefore, in principle, beneficial to the economic success of the geothermal operation. It is also a threat given the seismic hazard posed to local residents and infrastructures. As a matter of fact, a number of projects have been abandoned because of the incapacity of operators to control induced seismicity. There is therefore much need for operational methods to forecast seismicity during stimulation and production.

This issue has been an area of active research for several decades and different forecasting methods have been proposed [see for example the review by Gaucher et al. (2015)]. Some methods are based on a purely statistical data-driven approach while others include some of the physics involved in the triggering of induced seismicity by a fluid injection. A purely physics-based method is currently out of reach, as deterministic simulations would require knowledge of the heterogeneities properties of the sub-surface, in particular the distributions of stress and strength, with a level of details that cannot be constrained with observations. These heterogeneities are essential to reproduce well-established statistical properties of earthquakes such as their magnitude-frequency distribution (the so-called Gutenberg-Richter law) and need to be accounted for. Some idea of the fluid transport properties of the reservoir and their evolution during the stimulation would also be needed. In any case, progress on this issue hinges primarily upon the availability of quality observations as we use here, and the development of computationally efficient physics-based model. capable of reproducing the observations.

In this study, we analyze a seismological dataset acquired during an EGS development on Aalto University's Otaniemi campus by the Finnish company *St1 oy*. The 1st phase of the development consisted of 50 days of stimulations at 6.1 km deep. The stimulations were monitored with surface and borehole seismometers providing the possibility for excellent detection and location of the induced earthquakes (Kwiatek *et al.*, 2019, Hillers *et al.*, 2020). The stimulation included numerous phases of shut-in with different duration and of injection at different rates. This particular design turned out particularly helpful to investigate how the seismicity relates to the injection as we describe in the second section.

In the first section hereafter, we present a seismicity catalog produced with Machine Learning techniques. We next demonstrate that the seismicity can be reasonably well forecasted using a simple convolution model. In the third section we present simple physic-based simulations, which provide support for the validity of the convolution model. We finally discuss the implications for earthquake forecasting, and for optimization and control of geothermal stimulation and production.

2. EGS STIMULATION SETTING AND SEISMICITY DATA

2.1 Setting of the EGS stimulation

The injection well, OTN3c, was drilled into the Precambrian crystalline rocks and reached a depth of 6.1km (Figure 1). The last uncased 1000 m of OTN3c, which is inclined at 45°, was divided into several injection intervals. A total of 18,159 m^3 of water was injected during a period of 49 days between June 4th and July 24th, 2018 with wellhead pressures between 60 and 90 MPa and injection rates between 400 and 800 l/min. The stimulation was monitored in near-real time using an array of seismometers deployed at 2.20-2.65 km depth in another well, OTN2, located ~10 m from OTN3c and a 12-station network installed in 0.3-1.15 km deep wells (Figure 1). The reader is referred to Kwiatek et al. (2019) for more details.
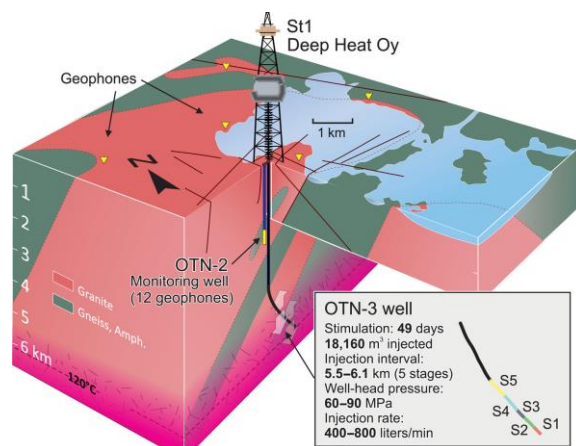

Figure 1: Setting of EGS stimulation on Aalto University's Otaniemi campus and seismological monitoring system (Kwiatek *et al.*, 2019) .

2.2 Data Processing

The data processing consists of three steps that we detail below: phase detection, waveform stacking and earthquake location.

We used the Generalised Phase Detection (GPD) procedure of Ross et al. (2018) to determine the probability of a P- and S-wave arrivals. The neural network was trained using the manual picks of the South California Seismic Network (SCSN) which consists of three-component 100Hz instruments deployed at the surface. For consistency, the continuous seismic data from the Helsinki dataset were resampled to 100Hz sample rate. The normalized probability of the P- and S-wave arrival was determined across the entire time-period of acquisition. These probabilities were then saved in a mini-seed format for a day of continuous seismic data for each station. The GPD only determines the probability of a phase arrival and not whether the various phase arrivals can be consistently associated to seismic events. To that effect we resorted to a backprojection technique (Smith *et al.*, 2020) using the open source software package QuakeMigrate (https://github.com/QuakeMigrate/QuakeMigrate). The P- and S-wave probability onset functions were back-propagated and stacked based the travel times calculated using a local 1D velocity. We used the velocity model of Kwiatek et al. (2019) based on the compilation of borehole logs from OTN-1 and OTN-3, regional P- and S-wave information and Vp/Vs ratios. The stacked values yield a four-dimensional grid in time and space of `coalescence' values with local maxima where the various P- and S-waves onset functions are consistent with a particular hypocentral location and origin time. We followed the procedure outlined in Smith et al. (2020) which provides a probabilistic estimate of these quantities: the four-dimensional grid is collapsed to a one-dimensional maximum coalescence value; an event is declared when this value exceeds median-average deviation value chosen to 11 as in Smith et al (2020).

Once events are detected, we take marginal windows of the four-dimensional grid about the maximum coalescence values, to determine an earthquake location and location uncertainty. As the GPD onsets are limited to 100Hz sampling rate, and represent a broad probability function of the phase arrivals, the earthquake location and uncertainties are poorly constrained at this stage of the procedure. The GPD onset functions are replaced with a STA/LTA (Short Term Average, Long term Average) sampled at 500Hz. These sharper onset functions were then used to determine normalized coalescence marginal window for each event. Figure 2 shows an example of the output of this procedure applied to the recordings of a M~1.3 event from both the surface and the OTN-2 deep borehole seismometers.

From this procedure, we produced a catalogue of 71,955 detected events, including 11,208 events which could be located. For comparison, Kwiatek et al. (2019) detected 61,150 events using the same seismological data set, of which 2,179 could be located with the remaining events imposed at the OTN-3 end point. The cumulated number of earthquakes shows a clear correlation with the cumulated injected volume suggesting that this catalog is probably adequate to quantify seismicity rate variations during the stimulation. To understand the small scale fracture structure we apply cross-correlation and relative relocation using HypoDD on the 11,208 locatable earthquakes, returning 998 that are clustered close to the stimulated segments of the OTN-3 borehole (Figure 4).
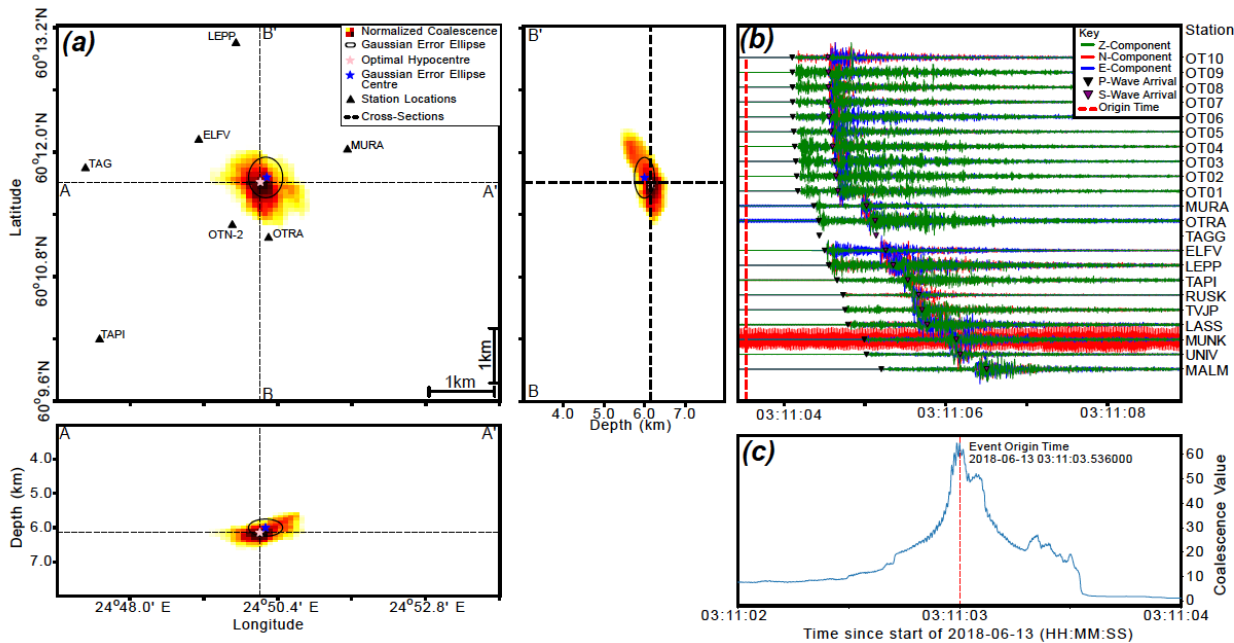
Figure 2: Event detection with QuakeMigrate. The M1.31event occurred on 3th June 2018 at 03:11:03. The location uncertainties in the E, N, and Z directions are estimated to 500m, 250m and 198m respectively (at the 67% confidence level, 1-σ). (a) Three-dimensional uncertainty in the earthquake location with 1error ellipse determined from the global covariance. (b) Seismograms with phase-picks (c) Probability distribution of the origin. Panels `c' represent the maximum coalescence value changing across the marginal window.
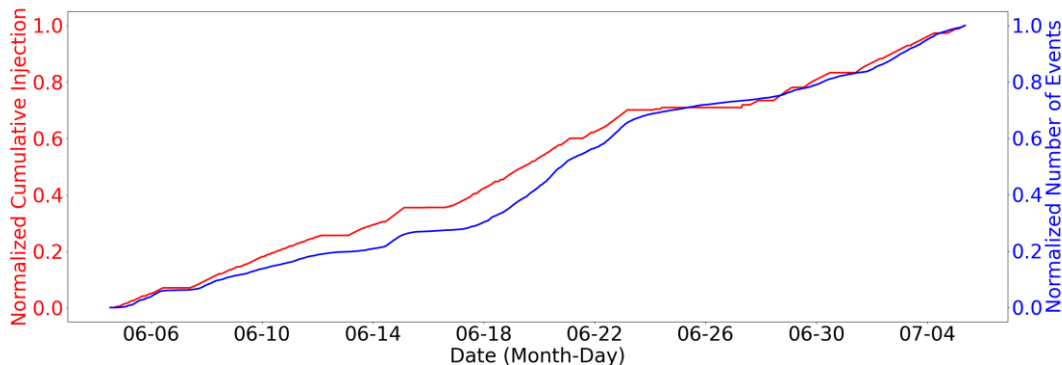

Figure 3: Normalized cumulated injected volume and normalized cumulated number of detected earthquakes over the first 30 days of stimulation.

The distribution of induced earthquakes shows that the volume with active seismicity extends typically ~200m away from the injection points (figures 4 & 5a). Fault reactivation, whether seismic or aseismic, is known to increase permeability (e.g., Guglielmi *et al.*, 2015). It is however possible that the seismicity extends beyond the zone where the permeability was significantly enhanced (Riffault *et al.*, 2018). In any case, how the cloud of seismicity relates to the hydraulically stimulated volume is not straightforward.

Figure 5a shows the distance of each event from the midpoint of the stimulated borehole segment at the time of the earthquake. It shows that the earthquakes occurred mostly within a few hundred meters from the injection point with no more than ~10% of the events at distances exceeding 1 km. When the data are split in different time bins we see that the distribution spreads away from the injection point (Figure 5b) as we would expect if seismicity is triggered by pore pressure diffusion (Shapiro *et al.*, 2006, Riffault *et al.*, 2018). By comparing these different distributions we estimated the diffusivity to 0.22 m2/s. The data collapse to a single, tighter distribution if distances are normalized to account of the effect of diffusion effect (Figure 5c). Some of the distant events however occurred early on suggesting that they are mislocated or reflect distant triggering by poro-elastic effects as has been observed also in the context of earthquakes induced by injection of wastewater (Goebel and Brodsky, 2018).
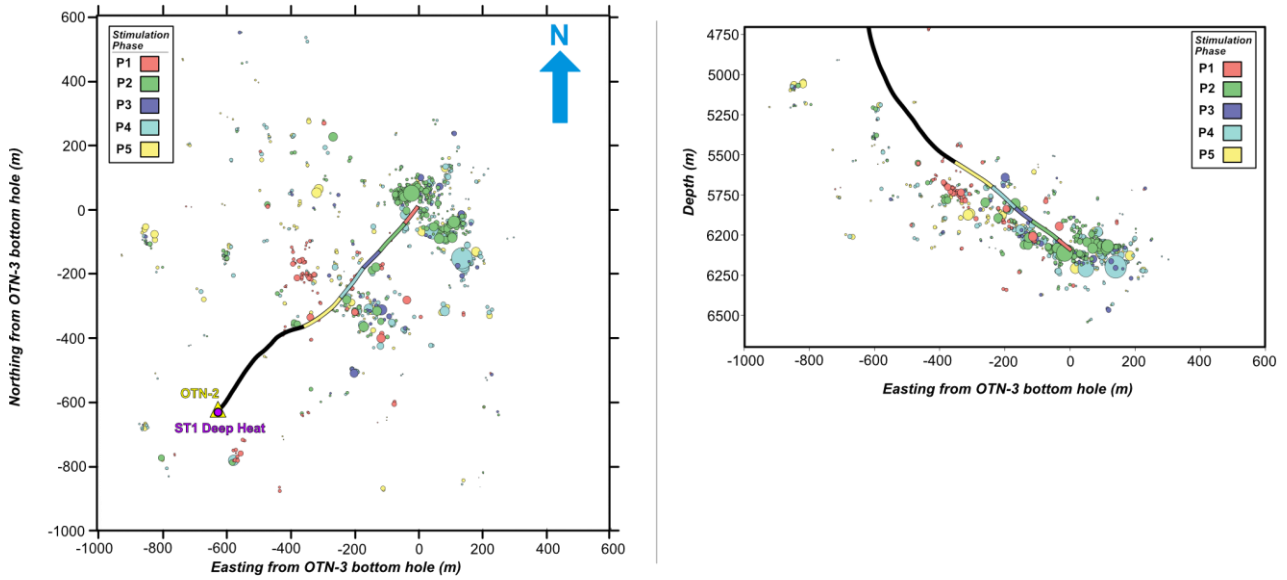
3

Figure 4: Map (left) and vertical section (right) view of the OTN-3 well and induced seismicity. The stimulated sections of the well and earthquake symbols are color-coded according to the stimulated segment. Only the 998 well located events are plotted here.
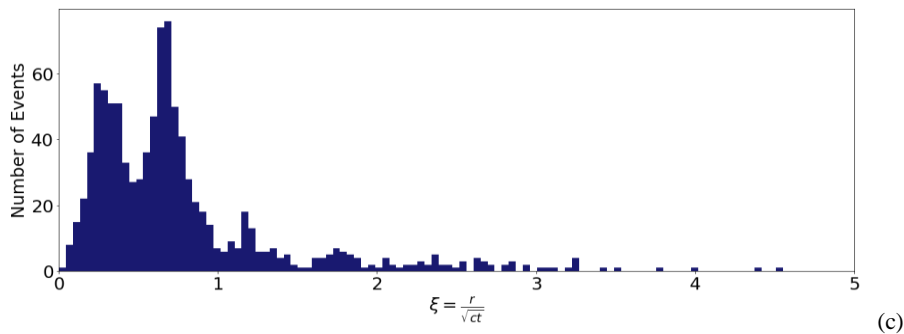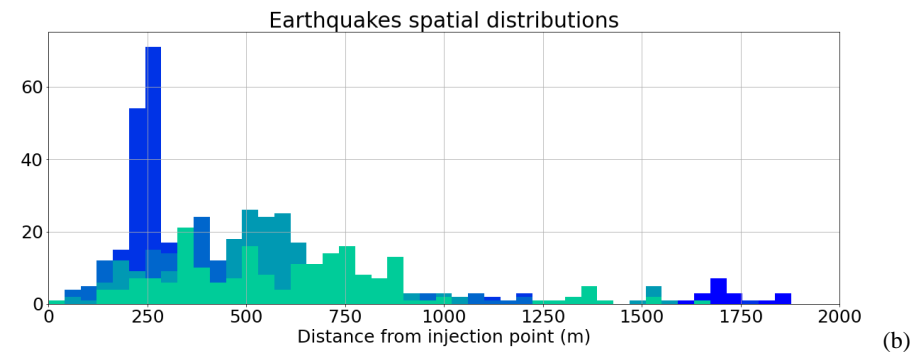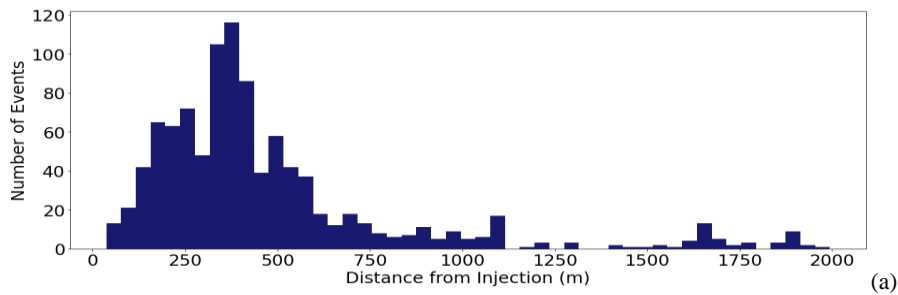

(a)

(b)

$$\xi = \frac{r}{\sqrt{ct}}$$

(c)

Figure 5: (a) Histogram of the distance of each well-located event from the midpoint of the stimulated borehole segment at the time of the earthquake. (b) Same plot for bins of 200 successive events. (c) Same as (a) with distance normalized with time since the beginning of the injection assuming a diffusivity of 0.22 m²/s.

Local magnitudes were estimated following Uski and Tuppurainen (1996), using the maximum amplitude from the Sg-Phase from a Wood-Anderson seismogram, hypocentral central distance, without any station corrections.

The magnitude-frequency distribution of induced earthquakes reported in our catalog (Figure 5) obeys the empirical Gutenberg-Richter law:

$$Log_{10}(N(> M)) = a - bM ,$$ (1a)

where $N(>M)$ is the cumulated number of earthquakes with local magnitude exceeding M. The magnitude of completeness, M_c, is estimated to -0.5. We estimate the b-value to 1.4+/-0.05 using the maximum likelihood method with account for the data binning (Marzocchi and Sandri, 2003). The data suggest a tapering at larger magnitude that might be statistically significant. This tapering could indicate a control of the extent of the larger ruptures by the size of the stimulated volume (Shapiro $et\ al.$, 2011). So we also considered the hypothesis of a tapered Gutenberg-Richter distribution, obtained by truncating the magnitude-frequency distribution at some maximum value M_{max}.

$$Log_{10}(N(> M)) = a - bM + Log_{10}(1 - 10^{b(M - M_{max})}) ,$$ (1b)

where $M < M_{max}$.

One difficulty of using the tapered Gutenberg-Richer distribution for forecasting is that, although it fits the observation better, M_{max} would need to be constrained a priori. In the following, we focus on analyzing and modeling how the seismicity rate depends on the injection history.
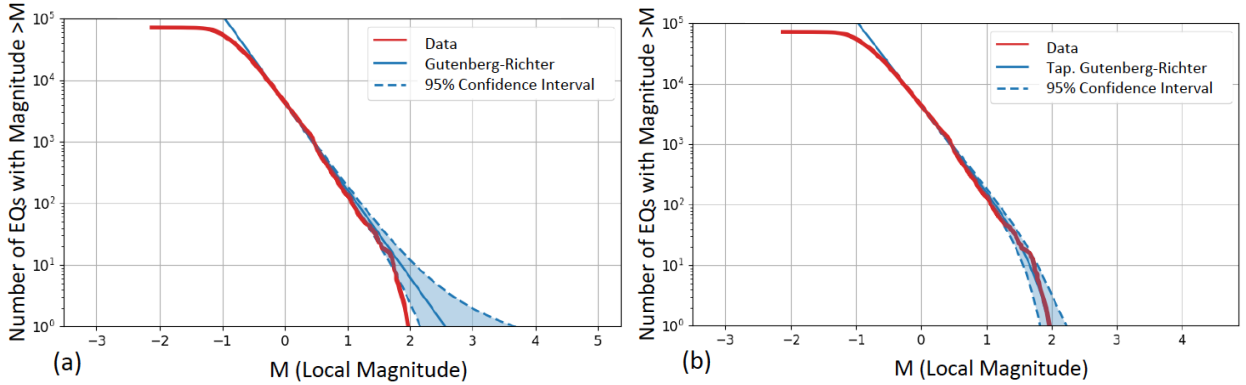

Figure 6: Frequency-magnitude distribution of earthquakes. The plots show in ordinate the cumulated number of earthquakes with magnitude exceeding the value indicated in abscissa. Blue line shows the best fitting Gutenberg-Richetr law (equation 1) determined from the maximum likelihood method using only M>0 events assuming (a) a Gutenberg-Richter distribution (equation 1a) or (b) a tapered Gutenberg-Richter distribution with $M_{max} = 2.0$ (equation 1b).

2. DATA ANALSIS AND MODELING

The seismicity is clearly governed by the injection history (Figure 3). It is clear however that the seismicity rate is not simply proportional to the injection rate, as is evident from a casual comparison of the variations of seismicity rate and injections rates (Figure 7). The seismicity ramps up, with some perceptible response time, at the onset of an injection and decays gradually when the injection stops. This behavior is not surprising as pore-pressure diffusion, poro-thermo elasticity stress transfer and earthquake nucleation and the initial strength distribution in the medium (the Coulomb stress needed to reach the condition for failure) are expected to result in a complex non-linear response (e.g., Langenbruch and Shapiro, 2010, Ader $et\ al.$, 2014, Segall and Lu, 2015, Mignan, 2016).

2.2 Post-injection seismicity rate decay

As has been observed in pervious studies (Bachmann $et\ al.$, 2012, Langenbruch and Shapiro, 2010), the decay during the shut-in periods follows approximately the Omori-law, which is usually used to describe the decay of aftershocks following large earthquakes (e.g., Utsu, 2002). In the case of our data (Figure 8), we find that the seismicity rate, R(t), follows quite well the standard Omori-law (p=1) after the end of the injection (set to t=0):

$$R(t) = \frac{R_0}{1 + t / t_a} ,$$ (2)

where R_0 is the initial rate (the seismicity rate at the end of the previous injection phase) and t_a is the relaxation time, defined as the time needed for the seismicity to decay to half its initial value.
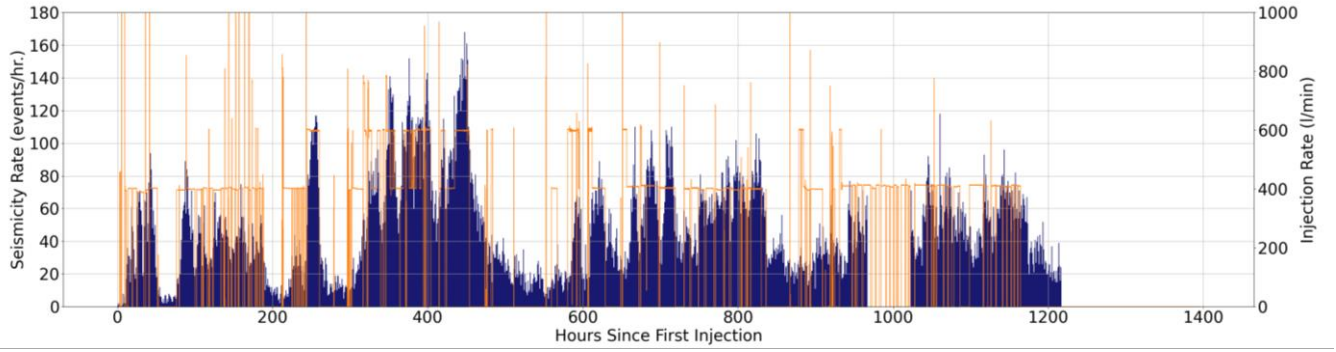
Figure 7: Evolution of the hourly seismicity rate and injection rate during the full stimulation period.
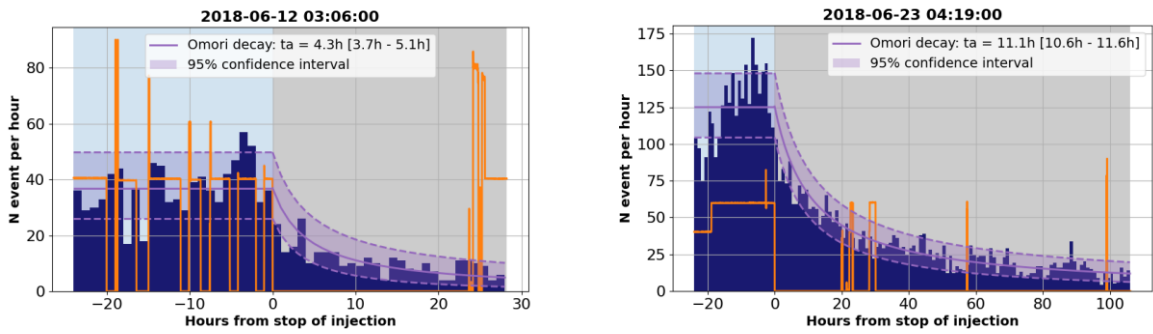

Figure 8: Omori-decay of seismicity rate during two different shut-in periods. The seismicity rate (blue bars) and injection (orange line) rate are plotted as in figure 7. The purple lines show the prediction from the Omori law (equation 2). Note that the relaxation time is ~ 3-4 h during the first example (on June 12, day 11) compared to ~11h during the second example (on June 23, day 19).

The mechanism at the origin of the Omori law remains poorly understood. It has been proposed that it would reflect the nucleation process of earthquakes (Dieterich, 1994), reloading by postseismic creep (Perfettini and Avouac, 2004) or postseismic fluid pressure relaxation (Miller, 2013, Nur and Booker, 1972). Simple models of earthquake nucleation and postseismic creep predict a p-value of~1, Similarly, pore pressure diffusion relaxation predicts a seismicity decay also closely resembling the Omori law with a p-value typically between 1 and 2 (Langenbruch and Shapiro, 2010, Miller, 2020). We find that the Omori law applies to our data reasonably. We additionally observe that the relaxation time increases throughout the stimulation and approximately linearly with time (Figure 9).
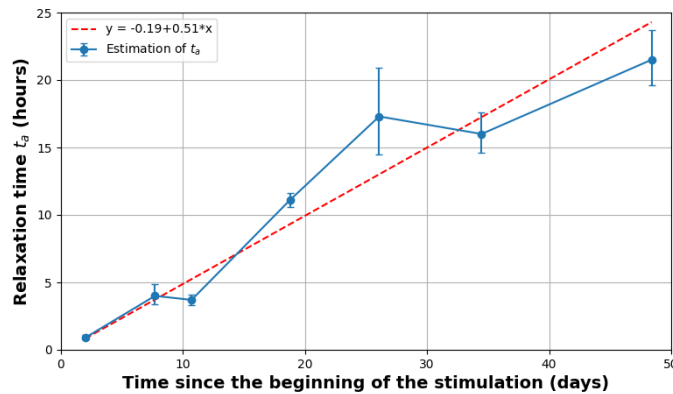

Figure 9: Evolution of the relaxation time during shut-in periods throughout the stimulation.

2.2 A simple convolution model

A physics-based model to forecast the seismicity due a geothermal injection would require accounting for thermo-poro-elasticity, the coupling between fracture activation and permeability changes, and some physical laws to describe the nucleation and growth of seismic ruptures. Despite significant advances in the modeling of some these aspects, there is no modeling framework yet available that would account for all of these mechanisms and which could be used to fit the observations. We therefore opt a simpler data-driven approach.

We assume that the earthquakes are driven by the stress changes induced by the injection (tectonic stress changes are assumed negligible) and that the fraction of earthquakes triggered by other earthquakes is negligible. We checked this assumption by analyzing the distribution of intervent distances in space and time using the method of Zaliapin and Ben-Zion (2013). The plot shows a unimodal distribution instead of the bimodal distribution that would be expected in case clustering due to aftershock sequences. This is consistent with the analysis by Kwiatek et al. (2019) shows that aftershocks account for no more than 10% of the events in their seismicity catalog and the common observations that aftershock sequences are rarely observed in seismicity induced by hydraulic stimulations (e.g., Baisch and Harjes, 2003). We additionally tested that the interevent time distributions is consistent with a Poisson point process. For a uniform Poisson process, we should see that interevent times are distributed following an exponential function. The rate of the Poisson process is not uniform in our case because the stressing rate must have varied in relation to the time history of the injection. We assume that, to first order, it is linearly related to the injection rate which allows substituting the injected volume of fluids for time. We therefore plot the histogram of volumes of fluids injected between successive events. The plot shows an exponential distribution consistent with a Poisson process with non-uniform rate proportional to the injection rate.
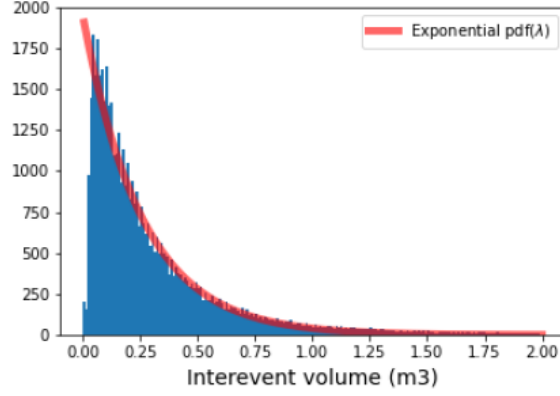

Figure 10: Distribution of injected volumes between successive events. The distribution is exponential as would be expected if the seismicity can be represented by a Poisson process with a rate proportional to the stress rate, assumed proportional to the injection rate. The rate of the resulting non uniform Poisson process expressed as a function of the injected volume (instead of time) is $\lambda=4$ events/m³.

The assumption of seismicity rate simply proportional to the injection rate would however would clearly fail to account of the lag of the seismicity response to the onset of injections and for the decay during shut-in periods. We therefore allow for a more complex relationship between seismicity and injection. Although the governing processes are certainly non-linear we make the assumption that they can be approximated to first order by a linear system. In that case, it should be possible to represent the physics relating the injection rate to seismicity rate with a transfer function. If so, the seismicity rate can be estimated from the convolution of the injection rate with the Green function representing the impulse response of the system:

$$R(t) = u(t) * g(t) = \int_{-\infty}^{+\infty} u(\tau) g(t - \tau)\, d\tau \tag{3}$$

where $R(t)$ is the seismicity rate, $u(t)$ is the injection rate and $g(t)$ is the Green function. We then need to estimate the Green function. Because the derivative of a step function is a Dirac function, it can be simply derived from the Omori-response to the stop of injection. We get:

$$g(t) = -\frac{d}{dt}\left(\frac{R_0}{1 + t/t_a}\right). \tag{4}$$

We additionally impose that t_a increases linearly with time during the stimulation:

$$t_a = a + bt, \tag{5}$$

where the coefficients α and β b are derived from the observations (Figure 9).

Note that with this assumption the system is not assumed time-invariant, the impulse response is actually time-dependent. Figure 11 shows that this approach provides a forecast that follows remarkably well the observed seismicity rate variations. The forecast accounts for the decay observed during the shut-in period, the lagged response to the onset of injections and the amplitude of the seismicity rate plateau reached during periods of constant injection rate.
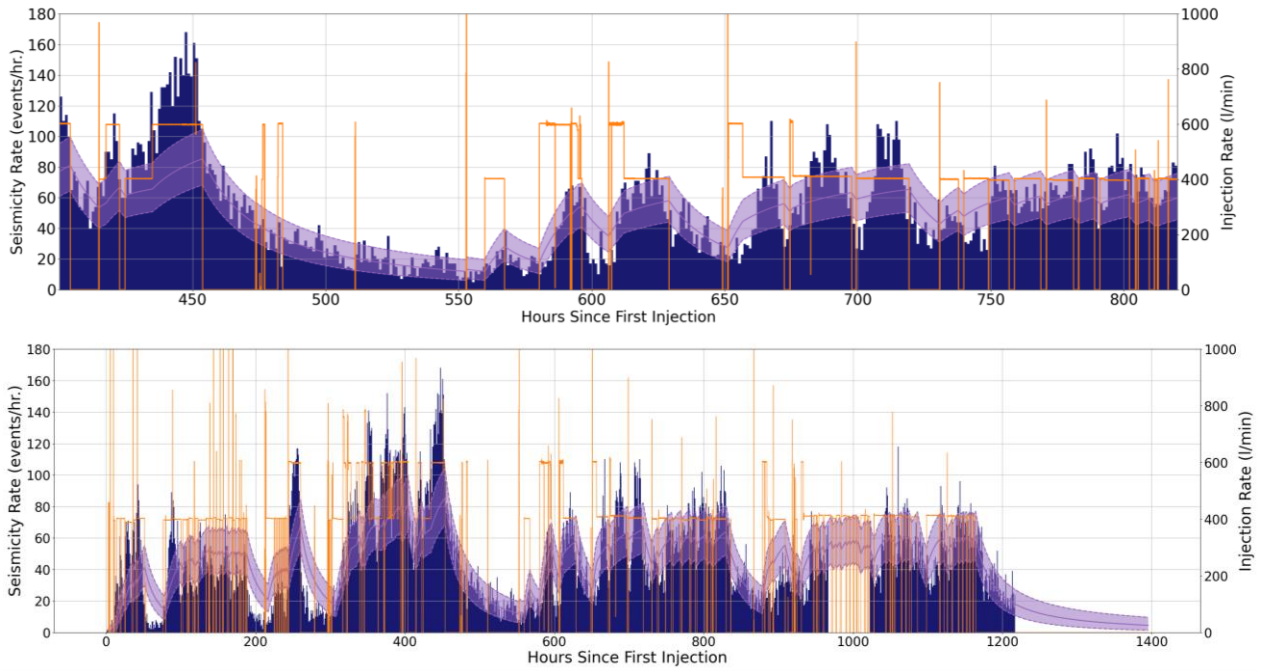
Figure 11: Comparison of the observed (blue bars) and predicted (purple curve with 95% confidence interval shaded) seismicity rate variations using the convolution model. Zoom in (top). Entire entire stimulation (bottom).

The model can then be used to estimate the expected maximum magnitude at any time or at any cumulated injected volume (Figure 12 a) or the probability of exceedance of a particular magnitude (Figure 12b). This calculation requires some assumption regarding the frequency-magnitude distribution of the earthquakes and regarding the distribution of their occurrence time. We tested both the standard and the tapered (for $M_{max}=2.0$) Gutenberg-Richter law. We use the parameters estimated from the entire dataset. So the model produces by design a cumulated number of earthquakes and a magnitude-frequency distribution of events consistent with the entire dataset. Figure 12 shows that the estimated maximum magnitude and the probability of exceedance of some depend strongly of the choice of the magnitude-frequency distribution. It should be noted that that the model ignores possible variations of the *b*-value.
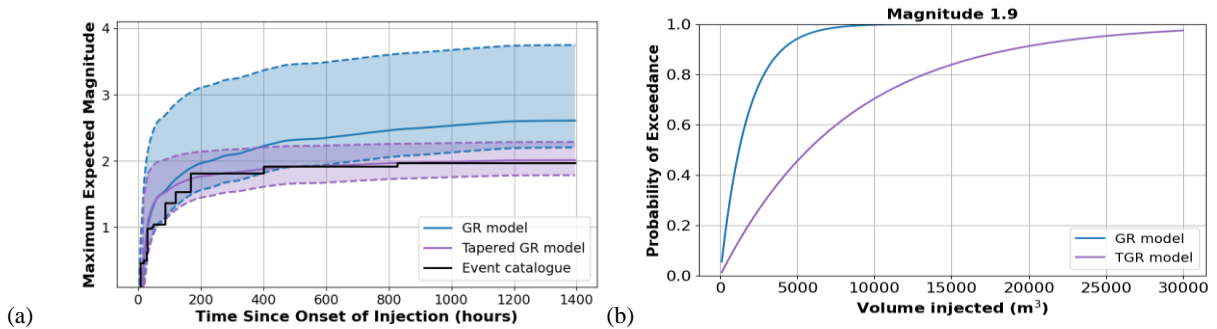

Figure 12: (a) Comparison of the observed and predicted maximum expected magnitude as a function of time assuming either the standard (GR, equation 1a) or the tapered (TGR, equation 1b) Gutenberg-Richter law. (b) Probability of the maximum magnitude exceeding M1.9 calculated with the two models as a function of the cumulated injected volume.

3. DISCUSSION

3.1 Performance of processing technique

This study demonstrates that deep learning algorithm of Ross et al. (2018), which was trained with observations from surface broadband seismic stations, performs very well when applied to data from borehole seismic stations. This is a remarkable result, which shows that the learning of P- and S-waves detection achieved with this algorithm on relatively large earthquakes (M > 3) recorded at regional distances (> 10 km) is transferrable to earthquakes of much lower magnitudes (<2.0) and recorded at small distances (<5km) with very different instruments. As more data from such experiments become available its is probable that the performance of the technique can be improved further. Retraining of the machine learning approach on more a larger data set of induced seismicity should remove the need of resorting to STA/LTA to refine the onset functions.

3.2 Justification of the convolution model through comparison with physics-based models

Here we test the convolution model on a synthetic catalog calculated using a simple hybrid simulator.

Different studies have developed models of earthquakes driven by pore-pressure diffusion due to a point injection in a poroelastic medium (Shapiro, 2018, Segall and Lu, 2015). Here we adopt a simplified version of such models. We calculate the pore-pressure diffusion in a homogeneous poro-elastic medium with constant permeability following the procedure of Segall and Lu (2015) (see parameters listed in Table 1). The model ignores the pore-pressure effect due to poro-elastic coupling. The seismicity rate on average in the domain is simply:

$$\frac{dN}{dt} = \frac{1}{\alpha} \iiint_V \frac{dp}{dt} \, dx \, dy \, dz$$

$$\text{,} \tag{6}$$

where N is the cumulated number of earthquakes, p is pore pressure, t is time, and α is a constant that is calibrated so that the total number of earthquakes over the modeled domain, V, matches the number of earthquakes in the observations.

In that case the pore-pressure variations relate linearly to the injection rate and depend only on the distance from the injection point and time (Figure 13). The parameters are listed in Table 1 and were chosen within the typical range of values found in the literature and so as to produce a synthetic seismicity catalog with characteristics similar to the observations.

Table 1: Model parameters.

Parameter	Variable	Value & Unit
Poroelastic Properties		
Shear Modulus	G	20 GPa
Drained Poisson's Ratio	ν	0.25
Undrained Poisson's Ratio	ν_u	0.3
Skempton's Coefficient	B	0.75
Biot's Coefficient	α	0.31
Transport Properties		
Permeability	k	1×10^{-15} m^2
Fluid Viscosity	η	0.4×10^{-3} Pa s
Hydraulic Diffusivity	c	9.1×10^{-2} m^2/s
Reference Fluid Density	ρ_0	10^3 kg/m^3
Friction Properties and Stress State		
Nominal Friction	μ_x	0.6
Effective Normal Stress	$\sigma_n - p$	16.7 MPa

We suppose that earthquakes occur on faults with constant orientations and are triggered when the standard Coulomb failure criterion is met:

$$S_s = S_0 + m_s (S_n - p), \tag{7}$$

where σ_n is the normal stress, σ_n is the shear stress, is σ_0 the cohesion, and μ_s is the internal friction angle of the material. Because we ignore poroelasticity, normal stress and shear stress are constant and the Coulomb stress rate varies in proportion to the pore pressure changes only. We assume that earthquakes nucleate instantaneously, leading to a drop of friction from its static, μ_s, to its dynamic value, μ_d. We assume that they occur on faults with an initial distribution of shear stress uniform distributed between $\mu_s \sigma_n$ and $\mu_d \sigma_n$. With these assumptions, the seismicity rate is proportional to the rate of Coulomb stress increase if the Coulomb stress rate increases monotonically (Ader *et al.*, 2014). In our implementation, the seismicity rate is therefore assumed proportional to the Coulomb stress rate, if positive, and zero if negative. This means that our model ignores the Kaiser effect (e.g., Lavrov, 2003), which implies that the Coulomb stress reached in the past needs to be exceeded to trigger a seismic event.

We determine the ratio of the seismicity rate to the Coulomb stress rates so that the mode produces the same number of earthquakes as observed with a injection history identical to that of the Deep Heat project. For simplicity, we assume that all the injections occur at the same point. Figure 13 shows the evolution of the seismicity rate as a function of time and space predicted by this model. Figure 14 shows a synthetic catalog of 70,000 events derived from random draw assuming a non-uniform Poisson process with the seismic rate predicted from the model. We next approximate the output of the simulator with the convolution model, assuming an Omori decay during shut-in periods.

We observe that the convolution model reproduces the synthetic data quite well (Figure 14). In particular, the model predicts a seismicity rate decay during shut-in periods that closely matches the Omori Law. This supports the claim that the Omori law does not necessarily reflect time-dependent nucleation and could rather reflect pore-pressure relaxation. We also see that the hybrid model implies a slight increase of the relaxation time over the course of the stimulation although not as large as in the observations. We do however see some systematic mismatches that we don't see when the convolution model is compared with the observation.

The most obvious discrepancy is that the synthetic catalogue does not show the lagging response to the injection that is observed in the data and predicted by the convolution model. One possible explanation might be that earthquake nucleation is not instantaneous. The inclusion of a time-dependent nucleation process would result in a damped response at the onset of injection that would better resemble the response observed in reality and the prediction from the convolution model. The Kaiser effect could also explain the discrepancy. It is not included in our synthetic data but it might well be present in the real data. This effect has indeed been reported in a number of hydraulic stimulation experiments (Zang *et al.*, 2014, Baisch and Harjes, 2003). Another possibility would be that the assumed uniform initial stress distribution is incorrect with in reality fewer faults close to failure than assumed in our model.

The expected time-evolution at the onset of an injection depends indeed strongly on the probability distribution function of the assumed initial stress (Langenbruch and Shapiro, 2010).

Another difference between the synthetic catalog and the real data is that the initial seismicity response is stronger than predicted by the convolution model while the opposite is observed with the real data (Figure 11).

Further work is needed to clarify the reasons for the differences between the observations and the prediction from the simulator. We haven't yet explored the impact of the various mechanisms that can be introduced in the model and are probably at play in reality. These include the impact poro-elastic coupling, time-dependent nucleation, the Kaiser effect, the pdf of initial stress distribution, the sensitivity of permeability to strain. It is however reassuring the convolution model reproduces reasonably well the prediction from our simple simulator.
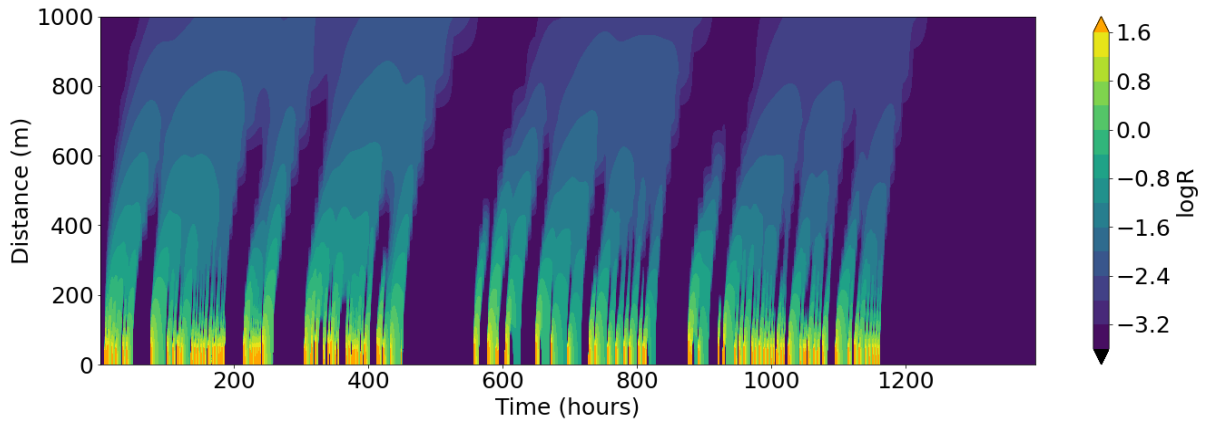

Figure 13: Spatio-temporal variations of the seismicity rate predicted by our model of seismicity driven by pore pressure diffusion in a linear-elastic medium for faults with a fixed orientation and assuming an injection history identical to the injection carried out during the ST1 Deep Heat Project on Otaniemi campus.
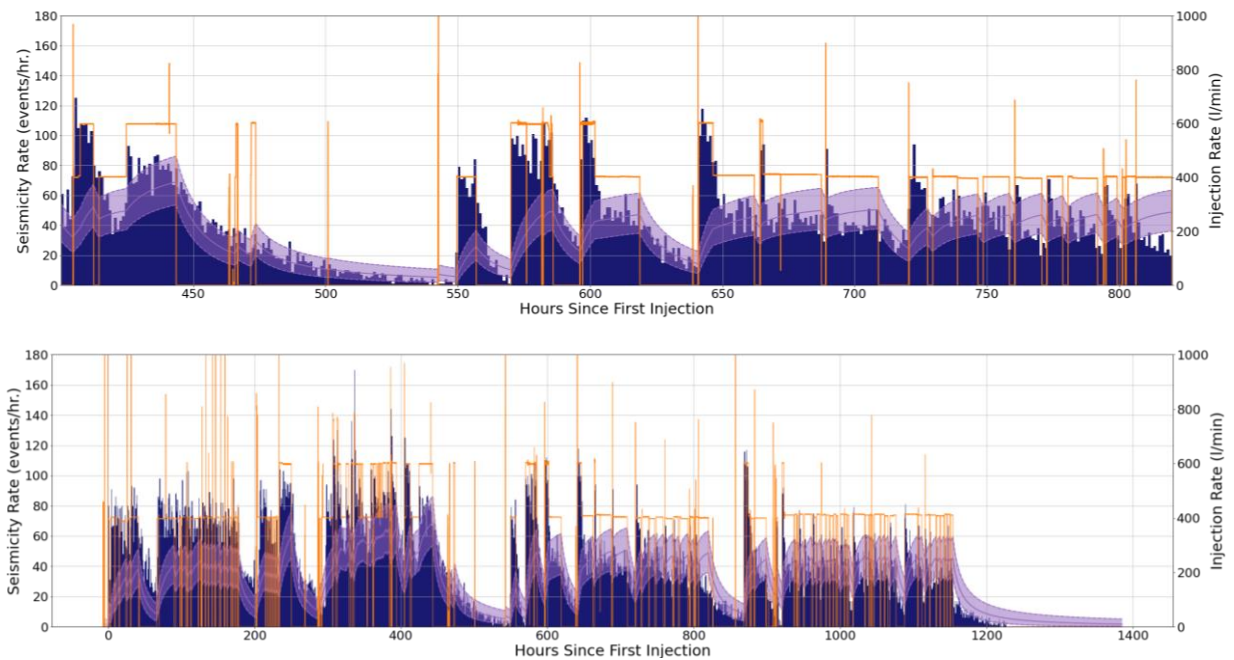

Figure 14: Comparison of the synthetic calatog (blue bars) and predicted (purple curve with 95% confidence interval shaded) seismicity rate variations using the convolution model. As an input we use the ST-OTN injection history. Zoom in (top). Entire entire stimulation (bottom).

3.3 Implication for operational forecasting, seismic hazard analysis or control and optimization.

The success of the convolution model at reproducing the seismicity observed during the Deep Heat stimulation on Otaniemi campus suggests that, at least in the particular setting of this experiment, the seismicity induced by the injection rate can be approximated by assuming a linear response of the natural system. If this approach is validated in other contexts, it would have important practical applications.

First the convolution model provides a conceptually simple and computational cost-effective framework for seismicity forecasting. It involves only a few parameters: there are 2 parameters if the relaxation time is assumed constant (the ratio of the seismicity rate to the injection rate and the relaxation time t_a; there are 4 parameters if t_a varies linearly varying with time. In this study we have used the entire data set to constrain the parameters of the model. In a real-time application one would need an a priori estimate of the parameters and some assimilation procedure to adjust them during the experiments. The quality of the forecast will depend on the amount of data available calling for the deployment of seismicity monitoring with a very low detection threshold such as what could be achieved with the seismometers deployed in the monitoring borehole during the Deep heat experiment. This would call also for a stimulation procedure specifically designed to probe the seismicity response of the reservoir, at least at the beginning of the stimulation. It should include sequences of injections at different rates separated by shut-in periods of appropriate duration to constrain the post-injection decay of seismicity which is critical for determining the transfer function of the system.

Once calibrated, the model could be used for time dependent seismic hazard assessment or to inform a traffic light system during the stimulation or the operation of a geothermal field. Traffic light systems based on actually recorded seismicity require a rather low threshold. False alarms are frequent which such systems due to the stochastic nature of the seismicity and the fact they depend exclusively on the magnitude of the extreme events. A traffic light system based on the probability of exceeding some threshold (in terms of magnitude or expected PGA or PGV at the surface) would be much less prone to false alarms and would take better advantage of the data collected during the stimulation. Figure 12b shows for example the probability of exceedance of a magnitude 1.9 event, which is typical of the magnitudes used in operational traffic light systems (Ader *et al.*, 2020). We see that it is very dependent of the choice of chosen parameterization of the frequency-magnitude distribution. Using a standard, non-tapered, Gutenberg-Richter distribution would provide a conservative upper bound. The use of tapered distribution might be more realistic in view of Figure 12a but would require a robust procedure or some a priori physical model to estimate M_{max}, (or the corner frequency of an unbounded representation of a tapered distribution) for example inspired from the model of Shapiro et al. (2011). The possibility that the b-value, or the maximum magnitude (or the corner magnitude) of a tapered model, night change during the operation would need to be accounted for. We haven't taken this possibility into account in this study.

Another application would the possibility to use the forecasting model for control and optimization of the injection rate during the stimulation or the operation of a geothermal well. Given the simplicity and linearity of the model the implementation of a controlling scheme would be straightforward. In the context of such an application, it would be important to resort to an automated procedure with low detection threshold to monitor the seismicity, this could be achieved with the processing approach used in this study. The operator might be specifically concerned with controlling the stimulated volume and permeability changes. This application would thus benefit from a better understanding of how the seismicity relates to the permeability and from an extension of the convolution model to space. This could be achieved by using kernels in the convolution model that would account for how the seismicity resulting from an impulse injection varies in space. We tested a data-driven approach to retrieve the dependency of the kernel on distance form the injection using the approach of Marsan and Lengliné (2008). This approach was initially designed to retrieve the kernels representing the probability of an earthquake triggering another earthquake. We adapted it to determine the probability of injection 'impulse' triggering an earthquake. An injection 'impulse' is defined as the volume injected over 10 minutes. In that case, only the limited dataset of well located events (998 events) can be used. Figure 15 shows that we were able to retrieve the Omori and the seismicity rate decays approximately as r^{-4}. where r is the radial distance form the injection. The determination of the kernel function is however not very stable to the limited data set. Further work is needed to address this issue.
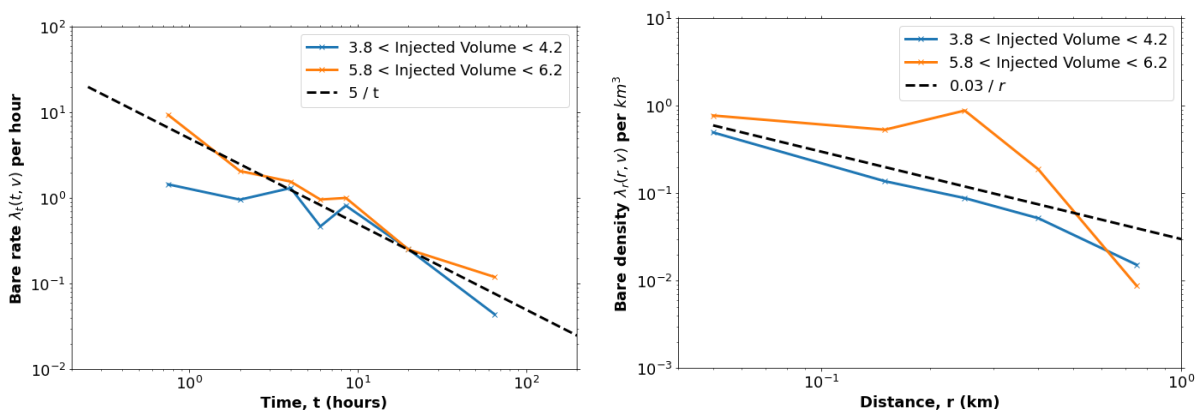

Figure 15: Kernel functions describing the seismicity rate as a function of time and distance following an 'impulse' injection derived from the data using the approach of Marsan and Lengliné (2008). Volumes are expressed in m^3. Only the 998 well located events (Figure 4) were used to inform the dependence of the kernel on distance (right panel).

5. CONCLUSION

The seismicity observations collected during the first phase of the Deep Heat EGS simulation on Otaniemi campus provide exceptional insight into how the temporal variation of seismicity rate relate to the injection rate, in particular because of the deployment of seismic array in a monitoring borehole but also because of a stimulation procedure which included numerous shut-in periods and different injection rates.

We observed that despite the complicated, presumably non-linear, physics at play, a simple convolution model can be used to estimate the temporal evolution of the seismicity rate as a function of the injection rate. We show that this approximation also applies to a synthetic catalog generated using a theoretical model of earthquakes driven by pore-pressure diffusion and obeying a standard Coulomb failure criterion with instantaneous nucleation. Further work is needed to test the general applicability of this approach. We need to explore under which conditions the convolution model is valid and how the parameters relate to the characteristics f the reservoir. This approach could in principle be used for seismic hazard assessment, to feed a traffic light system or eventually for optimization and control during stimulation.

REFERENCES

Ader, T., Chendorain, M., Free, M., Saarno, T., Heikkinen, P., Malin, P.E., Leary, P., Kwiatek, G., Dresen, G., Bluemle, F. & Vuorinen, T., 2020. Design and implementation of a traffic light system for deep geothermal well stimulation in Finland, *Journal of Seismology,* 24**,** 991-1014.

Ader, T.J., Lapusta, N., Avouac, J.-P. & Ampuero, J.-P., 2014. Response of rate-and-state seismogenic faults to harmonic shear-stress perturbations, *Geophysical Journal International,* 198**,** 385-413.

Bachmann, C.E., Wiemer, S., Goertz-Allmann, B.P. & Woessner, J., 2012. Influence of pore-pressure on the event-size distribution of induced earthquakes, *Geophysical Research Letters,* 39.

Baisch, S. & Harjes, H.P., 2003. A model for fluid-injection-induced seismicity at the KTB, Germany, *Geophysical Journal International,* 152**,** 160-170.

Dieterich, J.H., 1994. A constitutive law for the rate of earthquake production and its application to earthquake clustering, *J. Geophys. Res.,* 99**,** 2601-2618.

Elsworth, D., Fang, Y., Gan, Q., Im, K.J., Ishibashi, T. & Guglielmi, Y., 2016. *Induced seismicity in the development of EGS-benefits and drawbacks,* edn, Vol.

Gaucher, E., Schoenball, M., Heidbach, O., Zang, A., Fokker, P.A., van Wees, J.D. & Kohl, T., 2015. Induced seismicity in geothermal reservoirs: A review of forecasting approaches, *Renewable & Sustainable Energy Reviews,* 52**,** 1473-1490.

Goebel, T.H.W. & Brodsky, E.E., 2018. The spatial footprint of injection wells in a global compilation of induced earthquake sequences, *Science,* 361**,** 899-903.

Guglielmi, Y., Elsworth, D., Cappa, F., Henry, P., Gout, C., Dick, P. & Durand, J., 2015. In situ observations on the coupling between hydraulic diffusivity and displacements during fault reactivation in shales, *Journal of Geophysical Research-Solid Earth,* 120**,** 7729-7748.

Hillers, G., Vuorinen, T.A.T., Uski, M.R., Kortstrom, J.T., Mantyniemi, P., Tiira, T., Malin, P.E. & Saarno, T., 2020. The 2018 Geothermal Reservoir Stimulation in Espoo/Helsinki, Southern Finland: Seismic Network Anatomy and Data Features, *Seismological Research Letters,* 91**,** 770-786.

Kwiatek, G., Saarno, T., Ader, T., Bluemle, F., Bohnhoff, M., Chendorain, M., Dresen, G., Heikkinen, P., Kukkonen, I., Leary, P., Leonhardt, M., Malin, P., Martinez-Garzon, P., Passmore, K., Passmore, P., Valenzuela, S. & Wollin, C., 2019. Controlling fluid-induced seismicity during a 6.1-km-deep geothermal stimulation in Finland, *Science Advances,* 5.

Langenbruch, C. & Shapiro, S.A., 2010. Decay rate of fluid-induced seismicity after termination of reservoir stimulations, *Geophysics,* 75**,** MA53-MA62.

Lavrov, A., 2003. The Kaiser effect in rocks: principles and stress estimation techniques, *International Journal of Rock Mechanics and Mining Sciences,* 40**,** 151-171.

Majer, E.L., Baria, R., Stark, M., Oates, S., Bommer, J., Smith, B. & Asanuma, H., 2007. Induced seismicity associated with enhanced geothermal systems, *Geothermics,* 36**,** 185-222.

Marsan, D. & Lengline, O., 2008. Extending earthquakes' reach through cascading, *Science,* 319**,** 1076-1079.

Marzocchi, W. & Sandri, L., 2003. A review and new insights on the estimation of the b-value and its uncertainty, *Annals of Geophysics,* 46**,** 1271-1282.

Mignan, A., 2016. Static behaviour of induced seismicity, *Nonlinear Processes in Geophysics,* 23**,** 107-113.

Miller, S.A., 2020. Aftershocks are fluid-driven and decay rates controlled by permeability dynamics, *Nature Communications*.

Miller, S.A., 2013. The Role of Fluids in Tectonic and Earthquake Processes. *in Advances in Geophysics, Vol 54*, pp. 1-46, ed. Dmowska, R.

Nur, A. & Booker, J.R., 1972. Aftershocks Caused By Pore Fluid-Flow, *Science,* 175**,** 885-&.

Perfettini, H. & Avouac, J.P., 2004. Postseismic relaxation driven by brittle creep: A possible mechanism to reconcile geodetic measurements and the decay rate of aftershocks, application to the Chi-Chi earthquake, Taiwan, *Journal of Geophysical Research-Solid Earth,* 109.

Riffault, J., Dempsey, D., Karra, S. & Archer, R., 2018. Microseismicity Cloud Can Be Substantially Larger Than the Associated Stimulated Fracture Volume: The Case of the Paralana Enhanced Geothermal System, *Journal of Geophysical Research-Solid Earth,* 123**,** 6845-6870.

Ross, Z.E., Meier, M.A., Hauksson, E. & Heaton, T.H., 2018. Generalized Seismic Phase Detection with Deep Learning, *Bulletin of the Seismological Society of America,* 108**,** 2894-2901.

Segall, P. & Lu, S., 2015. Injection-induced seismicity: Poroelastic and earthquake nucleation effects, *Journal of Geophysical Research-Solid Earth,* 120**,** 5082-5103.

Shapiro, S.A., 2018. Seismogenic Index of Underground Fluid Injections and Productions, *Journal of Geophysical Research-Solid Earth,* 123**,** 7983-7997.

Shapiro, S.A., Dinske, C. & Rothert, E., 2006. Hydraulic-fracturing controlled dynamics of microseismic clouds, *Geophysical Research Letters,* 33.

Shapiro, S.A., Kruger, O.S., Dinske, C. & Langenbruch, C., 2011. Magnitudes of induced earthquakes and geometric scales of fluid-stimulated rock volumes, *Geophysics,* 76**,** WC55-WC63.

Smith, J.D., White, R.S., Avouac, J.P. & Bourne, S., 2020. Probabilistic earthquake locations of induced seismicity in the Groningen region, the Netherlands, *Geophysical Journal International,* 222**,** 507-516.

Uski, M. & Tuppurainen, A., 1996. A new local magnitude scale for the Finnish seismic network, *Tectonophysics,* 261**,** 23-37.

Utsu, T., 2002. Statistical features of seismicity, *International handbook of earthquake and engineering seismology, Part B***,** 719–732.

Zaliapin, I. & Ben-Zion, Y., 2013. Earthquake clusters in southern California I: Identification and stability, *Journal of Geophysical Research-Solid Earth,* 118**,** 2847-2864.

Zang, A.N., Oye, V., Jousset, P., Deichmann, N., Gritto, R., McGarr, A., Majer, E. & Bruhn, D., 2014. Analysis of induced seismicity in geothermal reservoirs - An overview, *Geothermics,* 52**,** 6-21.